atoms

MDPI

Article

EWS Time Delay in Low Energy $e-C_{60}$ Elastic Scattering

Aiswarya R. [1], Rasheed Shaik [2], Jobin Jose [1,*], Hari R. Varma [2] and Himadri S. Chakraborty [3]

[1] Department of Physics, Indian Institute of Technology Patna, Bihta 801103, Bihar, India; aiswarya_2121ph01@iitp.ac.in
[2] School of Physical Sciences, Indian Institute of Technology Mandi, Mandi 175005, Himachal Pradesh, India; rasheedskr@gmail.com (R.S.); hari@iitmandi.ac.in (H.R.V.)
[3] Department of Natural Sciences, Dean L. Hubbard Center for Innovation, Northwest Missouri State University, Maryville, MO 64468, USA; himadri@nwmissouri.edu
* Correspondence: jobin.jose@iitp.ac.in

Abstract: Access to time delay in a projectile-target scattering is a fundamental tool in understanding their interactions by probing the temporal domain. The present study focuses on computing and analyzing the Eisenbud-Wigner-Smith (EWS) time delay in low energy elastic $e-C_{60}$ scattering. The investigation is carried out in the framework of a non-relativistic partial wave analysis (PWA) technique. The projectile-target interaction is described in (i) Density Functional Theory (DFT) and (ii) Annular Square Well (ASW) static model, and their final results are compared in details. The impact of polarization on resonant and non-resonant time delay is also investigated.

Keywords: Eisenbud-Wigner-Smith (EWS) time delay; average time delay; Density Functional Theory (DFT) model; Anullar Square Well (ASW) model; resonance

Citation: Aiswarya R.; Shaik, R.; Jose, J.; Varma, H.R.; Chakraborty, H.S. EWS Time Delay in Low Energy $e-C_{60}$ Elastic Scattering. *Atoms* **2024**, *12*, 18. https://doi.org/10.3390/atoms12030018

Academic Editor: Kanti M. Aggarwal

Received: 26 December 2023
Revised: 13 March 2024
Accepted: 17 March 2024
Published: 21 March 2024

1. Introduction

The unprecedented developments in the field of attosecond chronoscopy have enabled scientists to follow electron dynamics with very high precision. This is possible due to the pioneering experimental studies carried out by Pierre Agostini, Ferenc Krausz, and Anne L'Huillier for which they were awarded the 2023 Nobel prize in Physics. The related comprehensive developments in research marked the birth of a new sub-field, atto-science, in the vast landscape of ultrafast science. As a result, many of the fundamental interactions, initially considered as instantaneous processes are found to be associated with some delay or acceleration of the order of attoseconds. For example, Krausz and coworkers [1] have shown that electron emission from the $3p$ orbital of the Ne atom has a temporal delay of 21 ± 5 attoseconds when compared to the delay from the $3s$ orbital. This finding instigated numerous theoretical and experimental investigations in time delay studies that explored features associated with photoionization dynamics.

Surprisingly, not many studies, in the wake of these developments, were reported on the particle scattering processes in the temporal domain, with the exception of a few studies by Amusia et al. [2–4]. The idea of time delay was initially proposed in the context of electron-scattering by Eisenbud [5], Wigner [6], and Smith [7]. Later, a few notable studies analyzed temporal dynamics in scattering [2,8,9]. The Eisenbud-Wigner-Smith (EWS) time delay is defined as the energy derivative of the scattering phase shift and it is an observable quantum mechanical parameter [1,10–12]. The understanding of the EWS time delay in a scattering process provides important details. For example, shape resonances in the scattering cross-section demonstrate how the projectile–target complex interacts to produce a quasi-bound state, which results in a delay [13]. Studies on shape resonance have gained a lot of attention because of their widespread application in several fields of physics, including cold atom physics [14], biological research [15,16], condensed matter physics [17], quantum transportation [18], etc.

Over the years, many atomic and molecular targets have been analyzed using scattering techniques. Among these, fullerene-C_{60} has been the subject of a handful of spectroscopic investigations. C_{60}, having 12 pentagonal and 20 hexagonal carbon rings is an extremely stable molecule with a fascinating symmetry. Another similar class of molecular compounds, endohedral fullerenes [19,20] are fullerene cages with an atom or a molecule or an atomic cluster or a smaller fullerene inside them. These are denoted by A@C_N where N denotes the number of carbon atoms in the fullerene and A is the species trapped in the cage. Fullerene and endofullerene complexes have a wide range of practical applications, such as in cancer detection and treatment [21], medical imaging [22], organic photovoltaic devices [23,24], quantum computing [25], Hydrogen storage [26], etc. A rubidium atom inside a fullerene, commonly known as a Jahn-Teller metal, exhibits superconductivity at high-temperature [27]. Also, in interstellar environments, the traces of fullerenes and their ionic complexes have been detected [28–30].

Despite such widespread applications, the majority of the work on fullerenes is photoionization-based (see articles [10,31] and references therein). Recent studies have addressed time delays in the photoionization of fullerene [32,33] and endofullerene systems [34–36]. On the other hand, there are relatively limited theoretical or experimental studies investigating the elastic scattering of fullerene. A few notable molecular-level calculations on $e-C_{60}$ elastic scattering were accomplished by the group of McKoy [37,38] using Schwinger multichannel (SMC) method and by Gianturco et al. [39] employing static exchange-correlation polarization (SECP) potential model. On the experimental side, Tanaka et al. [40,41] performed low-energy elastic $e-C_{60}$ scattering, whereas Hargreaves et al. [38] investigated high-energy elastic scattering properties. All of these aforementioned studies focused on total, partial, and differential cross-sections. No experimental elastic scattering time delay study of C_{60} has been reported so far. On the theoretical side, a study by Amusia et al. [2] used the Dirac bubble potential model of fullerene to analyze the time delay, taking into account six partial waves. Additionally, a study conducted by Aiswarya and Jose [9], employing only the annular square well (ASW) model potential analyzed the EWS and angular delay in $e-C_{60}$ scattering.

The current work focuses on addressing the partial-wave averaged observable time delay properties and the effects of polarization on time delay, using more sophisticated modeling of fullerene based on Density Functional Theory (DFT) [42,43]. In addition, we use a static ASW model potential [44,45] for comparison purposes. In order to investigate the resonant delay features of $e-C_{60}$ scattering, the low-impact energy range is considered. In this range, the projectile electron wavelength is so large that the electron diffraction effects can be neglected. Theoretical aspects of the work are covered in Section 2, the results and associated discussions are presented in Section 3, and Section 4 concludes the report.

2. Theoretical Details

Assessing the suitability of $e-C_{60}$ interaction potential from the charge density at the fullerene shell was the main objective of the work of Baltenkov et al. [46]. They pointed out that the ASW potential has a nonphysical charge density for C_{60}, hence suggesting a diffused potential with a non-flat bottom and soft-edged walls to be more realistic. The $e-C_{60}$ potential simulated in this study using DFT has these attributes [46]. Thus, to capture the difference we compare and contrast the $e-C_{60}$ scattering time delay results using (1) ASW model [44] and (2) DFT potential generated within the local density approximation (LDA) [42,43]. The ASW potential is expressed as [44,45]:

$$V_{ASW} = \begin{cases} -U, & r_c - \frac{\Delta}{2} \leq r \leq r_c + \frac{\Delta}{2}, \\ 0, & otherwise \end{cases} \quad (1)$$

where the cage thickness Δ = 2.91 a.u., the mean radius r_c and well depth are, respectively, 6.71 a.u. and 0.2599 a.u. The ASW parameters were optimized to reproduce important physical properties of fullerene closely: Δ is twice the covalent radius of a carbon atom and

the well depth is adjusted to correspond with the electron affinity of −2.65 eV for $\ell = 1$ state of C_{60} [44]. In effect, therefore, the ASW potential is static, being oblivious to C_{60} electrons.

In the DFT model, the ionic core of fullerene is calculated within LDA where the potential (V_{jel}) [47] is obtained after considering sixty C_4^+ ions to be smeared and homogeneously distributed over a jellium shell of an average radius R of 6.70 a.u. A constant pseudo-potential was added for the quantitative accuracy [47]. The fullerene shell then optimizes self-consistently (see below) to a thickness Δ of 2.41 a.u. and a pseudo-potential value in order to ensure the charge neutrality and reproduce the measured first ionization threshold. The DFT-LDA potential for the $e-C_{60}$ interaction can be written as [42,43]:

$$V_{DFT}(r) = V_{jel}(r) + \int \frac{\rho(r')}{r - r'} dr' + V_{xc}(\rho(r)), \tag{2}$$

using which the Kohn–Sham equations [48] for a system of 240 electrons are solved self-consistently to obtain the ground-state electron density $\rho(r)$ [42]. The second and the third term on the right-hand side in Equation (2) represent the direct and the exchange-correlation interaction, respectively. The specific form of exchange-correlation potential used in the present study is [43]:

$$V_{xc}(\rho(r)) = -\left(\frac{3\rho(r)}{\pi}\right)^{1/3} - 0.0333 \ln\left[1 + 11.4\left(\frac{4\pi\rho(r)}{3}\right)^{1/3}\right]. \tag{3}$$

Here, the first and second terms on the right-hand side correspond to exchange and correlation potentials. The exchange term is derived from the Hartree–Fock (HF) formalism [43] in LDA. Obviously, the DFT potential extends beyond the static model to incorporate the C_{60} valence electron density within a mean field.

A realistic evaluation of the $e-C_{60}$ interaction requires accounting for polarization effects. As in the work by Dolmatov et al., the current study uses a static dipole polarization potential of the form [45,49]:

$$V_{pol} = \frac{-\alpha C_{60}}{2(r^2 + b^2)^2}. \tag{4}$$

In Equation (4), the static dipole polarizability $\alpha = 850$ a.u. and cut-off parameter $b = 8$ a.u. approximately includes the fullerene's radial extent. The final effective potential after the addition of polarization potential is:

$$V_{C_{60}}^{eff} = V_{DFT/ASW} + V_{pol}. \tag{5}$$

To illustrate the effect of polarization, V_{pol} is selectively included and omitted in the present study. Thus, four case studies are carried out: (1) ASW (ASW without polarization), (2) ASW-P (ASW with polarization), (3) DFT (DFT without polarization), and (4) DFT-P (DFT with polarization). All the respective potential shapes are shown in Figure 1. The ASW potential (Figure 1a) is altered by the introduction of the polarization potential, especially close to the fullerene center. The form of the DFT potential (Figure 1b) is innately of a diffused shape, and the addition of the attractive polarization potential makes the well slightly deeper. It may be emphasized that we have recently performed a comparison [50] of the $e-C_{60}$ elastic differential cross-section (DCS) using ASW-P and DFT-P with measurements and other competitive calculations. This has demonstrated that DFT is in better agreement with the experimental results than ASW, often performing better than even other theories. Furthermore, the success of jellium-DFT-based approaches in agreeing and interpreting experiments in other processes is known [42,51].

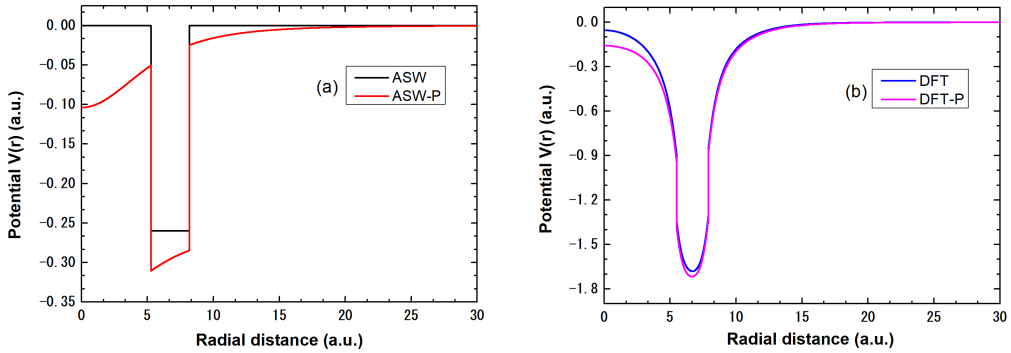

Figure 1. (**a**) ASW and (**b**) DFT model potentials with and without polarization effects.

A non-relativistic partial wave analysis (PWA) is carried out for all the cases considered. The scattered wave function of the electron after interacting with the C_{60} potential will be the solution of the following radial Schrödinger equation:

$$\left\{ \frac{-\hbar^2}{2m}\frac{d^2}{dr^2} + \left[V_{C_{60}}^{eff} + \frac{\hbar^2 \ell(\ell+1)}{2mr^2} \right] \right\} u_\ell(r) = E u_\ell(r). \tag{6}$$

Separate calculations are performed after decoupling the effect of polarization to investigate its impact. Using Numerov's method [52], the solution of Equation (6) is computed with the proper boundary conditions. Care is taken to ensure the continuity of the wave function and its derivative at the boundary of C_{60}. As in the earlier study [9], the elastic scattering phase shift (δ_ℓ) of the ℓ^{th} partial wave is obtained by considering the asymptotic form of the wave function [53]:

$$u_\ell(r > r_{max}) \propto kr[j_\ell(kr)cos\delta_\ell - n_\ell(kr)sin\delta_\ell]. \tag{7}$$

For any energy E of the projectile, the wave vector $k = \frac{\sqrt{2mE}}{\hbar}$. In Equation (7), j_ℓ and n_ℓ represent the Bessel function of the first and second kind, respectively, and r_{max} = 28 a.u. is taken as the practical infinity. Let r_1 and r_2 be the two radial points beyond r_{max}, using which phase shift (δ_ℓ) can be computed as [53]:

$$tan\delta_\ell(k) = \frac{\zeta j_\ell(kr_1) - j_\ell(kr_2)}{\zeta n_\ell(kr_1) - n_\ell(kr_2)} \tag{8}$$

with

$$\zeta = \frac{r_1 u_\ell(r_2)}{r_2 u_\ell(r_1)}. \tag{9}$$

The numerical values of j_ℓ and n_ℓ are generated using the well-established subroutines SPHJ and SPHY [54]. The partial waves with ℓ = 0–15 were determined to be sufficient for both the model potentials up to the energy of E = 0.5 a.u. considered in this study. Since most of the prominent resonances are observed in this energy range, the low-energy elastic $e-C_{60}$ scattering is addressed. Also, the current investigation has not included the inelastic scattering processes related to the $e-C_{60}$ interactions, such as the ionization, charge transfer, excitation, etc., since the energy range considered, 0–0.5 a.u. is much lower. These energies are also well below the C_{60} giant plasmon excitation energy (≈20 eV) [55]. Moreover, with such low projectile energies, and therefore, long enough de Broglie wavelengths, the electron cannot resolve the atomistic details of the target. This fact bodes well with the present models that omit the C_{60} ionic structures. At any rate, the total cross-section (TCS) of the elastic scattering is then given by [52,53]:

$$\sigma_{total} = \frac{4\pi}{k^2}\sum_{\ell=0}^{\infty}(2\ell+1)sin^2\delta_\ell. \tag{10}$$

The analysis of the quasi-bound states arising from distinct resonant partial-wave interactions with fullerene is performed using the Fano parametrization [56] formula:

$$\sigma_r = \frac{\sigma_o(q+\varepsilon)^2}{1+\varepsilon^2}, \tag{11}$$

with

$$\varepsilon = \frac{E - E_r}{\Gamma/2}. \tag{12}$$

In Equation (11), q is the shape parameter, σ_r and σ_o are the resonant and background cross-sections, respectively. Equation (12) provides the parameter ε, where Γ and E_r are the resonant width and energy, respectively. The time delay τ_ℓ of the ℓ^{th} partial wave is given by the EWS time delay formula [7]:

$$\tau_\ell(E) = 2\hbar\frac{\partial\delta_\ell}{\partial E} = 2\hbar\delta'_\ell. \tag{13}$$

The average time delay for a given potential is then computed by [2]:

$$\tau_{avg}(E) = \sum_{\ell=0}^{\infty} \frac{\sigma_\ell}{\sigma_{total}}\tau_\ell(E). \tag{14}$$

where σ_ℓ and τ_ℓ are, respectively, the partial cross-section (PCS) and time delay of the ℓ^{th} partial wave. We analyze the resonant time delay for all four case studies of the model potentials (see above). All the calculations are conducted in atomic units (a.u.) unless specified otherwise.

3. Results and Discussion

This section is divided into four subsections: Section 3.1 deals with the $e-C_{60}$ TCS and near-threshold behavior of the phase shift and time delay; Section 3.2 discusses the Fano parameterization of resonant partial waves. Resonant phase shifts and time delays are covered in Sections 3.3 and 3.4 presents the average time delay.

3.1. TCS and Near-Threshold Behavior of Phase Shift and Time Delay

The TCS of $e-C_{60}$ elastic scattering contributed by ℓ = 0–15 partial waves is shown in Figure 2. Cross-sections in the ASW and ASW-P model are shown in Figure 2a. In TCS, for the ASW case three prominent peaks are noted from the partial waves ℓ = 3, 4, and 5; $\ell = 3$ is the sharpest and closer to zero energy, while $\ell = 5$ is the weakest. This sharp resonance corresponding to $\ell = 3$ is not observed for the polarization-added ASW potential case (ASW-P). In this case, resonant peaks are mainly due to the contribution from partial waves ℓ = 4, 5, and 6. The inset features a magnified view of TCS at the near-zero energy region which shows the polarization induced $\ell = 0$ resonance that occurs right at the threshold. For the ASW potential, the addition of polarization effects shifts the resonance to lower energies. Thus, two common resonance peaks ($\ell = 4$ and 5) are noticed both in ASW and ASW-P. The TCS obtained using DFT and DFT-P potential models are shown in Figure 2b. Since the DFT simulated $e-C_{60}$ interaction potential has a deeper well depth than the ASW case, more resonances are formed. A zero-energy resonance is seen for the DFT potential, followed by a resonance corresponding to $\ell = 3$. For the polarization-added DFT model (DFT-P), a resonance for $\ell = 1$ is noted quite close to the threshold. A set of peaks corresponding to the partial waves $\ell = 4$, 7, 8, and 12 is seen both in DFT and DFT-P. When the polarization is added to the model potentials (ASW/DFT), a consistent trend is that the resonant partial wave peaks shift toward lower energies. This is because the presence of the attractive polarization potential results in a minor reduction in the angular momentum barrier, leading to the attainment of resonant conditions at slightly lower projectile energies.

From a physical perspective, the cross-section reveals the effective area offered by the target for the projectile to scatter off. From Figure 2 it can be noted that the background (non-resonant) cross-section in the DFT model is three times larger than that in the ASW model. This can be understood as follows. Firstly, the DFT potential shape is diffused offering effectively a larger cross-section area for scattering. Secondly, the strength of the attractive potential in the DFT model is more than in the ASW model.

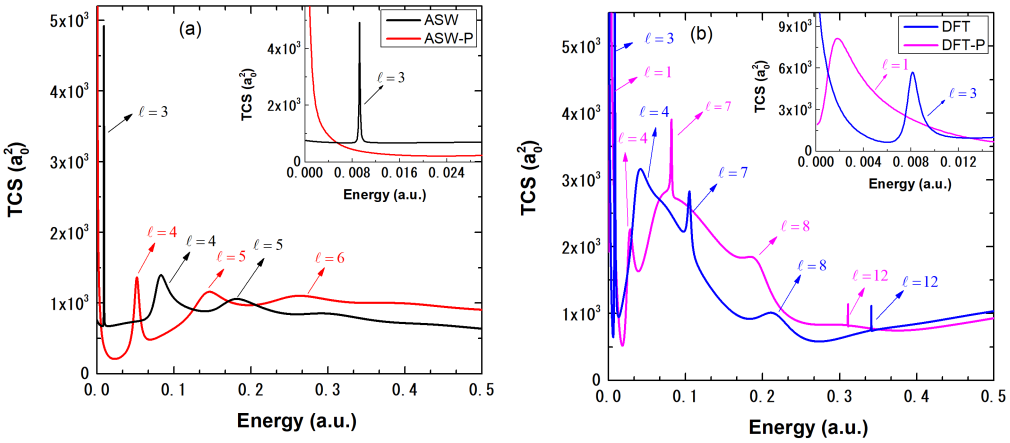

Figure 2. TCS of $e-C_{60}$ elastic scattering using (**a**) ASW (black) and ASW-P (red); (**b**) DFT (blue) and DFT-P (magenta). Resonances are labeled with corresponding partial wave numbers. The inset shows magnified TCS in the low-energy region.

Resonant and non-resonant TCS studies for the $e-C_{60}$ collision reported in the literature are aplenty, mostly using static model potentials [44,57,58] and a few others using molecular level calculations [37,39]. Table 1 presents a comparison between the resonant energies obtained from the present analysis using DFT-P and ASW-P with the other static potentials [44,57,58]. In general, an overall agreement for the number of resonances and the partial waves assigned is seen. On the other hand, Winstead and McKoy [37] and Gianturco et al. [39] have performed molecular-level investigations of $e-C_{60}$ scattering, reporting σ and π type resonances in the cross-section. In SMC calculations by Winstead and McKoy, the lowest $\pi-$ type resonance was obtained in the energy range of 0.0588–0.0955 a.u. with the h_u symmetry. A g_g resonance of π type is observed within the interval of 0.0919–0.1286 a.u., followed by a g_u resonance in the range of 0.1323–0.1691 a.u. The t_{2g} resonance occurs between 0.1654 a.u. and 0.2021 a.u., while the first and the second t_{1u} resonances are determined at 0.2279 a.u. and 0.2833 a.u., respectively. Also, a t_{2u} resonance near 0.2132 a.u. is noted. Two overlapping t_{1g} resonances are noticed at about 0.3565 a.u. In Gianturco et al.'s [39] SECP calculation, π type h_u resonance at 0.0797 a.u. was observed to be the lowest. This was followed by resonances in the order of a_g, g_g, g_u, t_{2g}, and t_{1u} at 0.1014 a.u., 0.1172 a.u., 0.2139 a.u., 0.2282 a.u., and 0.2102 a.u., respectively. The second t_{1u} resonance was observed at 0.2833 a.u., followed by a t_{1g} resonance at 0.2998 a.u. The first h_g resonance appeared at 0.2646 a.u., with a subsequent t_{2u} resonance identified at 0.3712 a.u. Interestingly, even though these resonances originate from molecular symmetry, their energy range of occurrences overlaps with the range of partial wave resonances in the current study. Furthermore, by the molecular level calculations, more resonances are obtained in the DFT model versus the ASW case. This is further evidence of the superiority of the DFT description of $e-C_{60}$.

Table 1. Resonant energy in a.u. using different model potentials.

	DFT-P	ASW-P	ASW [44]	GASW [57]	Lorentzian [57]	$\delta-$Shell [58]
Resonance 1	0.0013 ($\ell = 1$)	0.0524 ($\ell = 4$)	0.0107 ($\ell = 3$)	0.0691 ($\ell = 4$)	0.0908 ($\ell = 3$)	0.0364 ($\ell = 3$)
Resonance 2	0.0258 ($\ell = 4$)	0.1380 ($\ell = 5$)	0.0815 ($\ell = 4$)	0.1628 ($\ell = 5$)	0.1988 ($\ell = 4$)	0.1301 ($\ell = 4$)
Resonance 3	0.0818 ($\ell = 7$)	0.2350 ($\ell = 6$)	0.1835 ($\ell = 5$)		0.3359 ($\ell = 5$)	0.2738 ($\ell = 5$)
Resonance 4	0.1920 ($\ell = 8$)					
Resonance 5	0.3109 ($\ell = 12$)					

Figure 3 illustrates the near-threshold phase shift and EWS time delay behavior in ASW and DFT approximations; time delays are presented in attoseconds (as). In the zero energy limit, the phase shift and time delay follow the Wigner threshold law [59]. Since the s-wave phase shift behaves as $\delta_{\ell=0}(E \to 0) \propto \pi - E^{1/2}$, it approaches π as $E \to 0$, which is evident in the figure for the case of $\ell = 0$. The corresponding time delay goes to negative infinity $\tau_{\ell=0}(E \to 0) \propto -E^{-1/2}$, which is also clear in the bottom panel for $\ell = 0$. According to the Wigner threshold law, the phase shift for other partial waves $\ell \neq 0$ is $\delta_{\ell>0}(E \to 0) \propto \pm E^{\ell+1/2}$. Therefore, in this case, the phase shift should tend to zero in the zero-energy limit, as shown in the upper panel in Figure 3. The corresponding time delay must vanish for the partial waves $\ell > 0$ in the low energy limit, since $\tau_{\ell>0}(E \to 0) \propto \pm E^{\ell-1/2}$. Hence, the current set of results is consistent with the Wigner threshold law. Note, that the time delay in the present context is regarding a free unscattered electron. A positive time delay refers to a delay of scattered electrons reaching the detector compared to unscattered ones as if it feels like a transient attraction. Likewise, a negative time delay suggests the scattered electron is reaching the detector earlier than the reference electron. The latter is indicative of the electron receiving a repulsive push during the scattering.

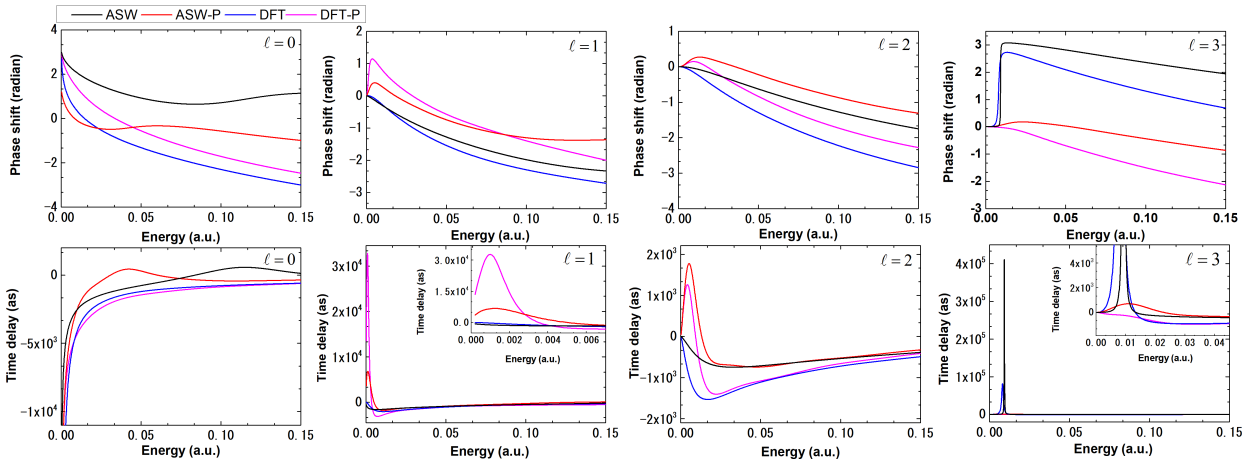

Figure 3. Phase shift (**upper panel**) and corresponding time delay (**lower panel**) in the near-zero energy range using ASW (black), ASW-P(red), DFT (blue) and DFT-P (magenta) model potentials. Inset shows the magnified view of the time delay for ℓ = 1 and 3.

We now investigate the low-energy behavior of phase shifts and time delays in the presence of the polarization effect. For each of $\ell = 1$ and 2, the phase shift is positive in the low-energy region in ASW-P and DFT-P compared to the unpolarized target approximation.

Consequently, there is a positive hump in the time delay for both these cases. We note that the polarization induces an attractive potential (Figure 1). Let us model the polarization effect parametrically by λ, which can be tuned to adjust the polarization potential. In the limit $\delta_\ell \to 0$, the relation between the phase shift and the potential can be approximated as [53]:

$$\frac{d\delta_\ell}{d\lambda} = -k \int_0^\infty [u_\ell(\lambda, r)]^2 \frac{\partial V_{C_{60}}}{\partial \lambda}\, dr, \tag{15}$$

where $u_\ell(\lambda, r)$ is the asymptotic radial wave function for the wave vector k. The rate of change of the strength of C_{60} potential upon the addition of the polarization effect is expressed by $\frac{\partial V_{C_{60}}}{\partial \lambda}$, which is negative in the present case. From Equation (15), it is evident that the associated phase shift variation has the opposite sign if the potential variation, $\frac{\partial V_{C_{60}}}{\partial \lambda}$, has the same sign for all values of r [53]. Analyzing the phase shift behavior for $\ell = 1$ and 2, we find that phase shifts from all four model potentials approach zero at very low energies, validating the Wigner threshold law. Furthermore, for model potentials where polarization is considered (ASW-P/DFT-P), the phase shift attains positive values, while for the bare cases (ASW/DFT) it grows in negative values. The reason for this behavior can be made clear from Equation (15). For the polarized target case, the value of $\frac{\partial V_{C_{60}}}{\partial \lambda}$ is more negative compared to the non-polarized case; hence, at a given k value, the scattering phase shift of the P case will be relatively more positive compared to the non-P case. Coming to the behavior of the time delay, we recall that τ_ℓ is obtained as the energy derivative of the δ_ℓ. As a result, for $\ell = 1$ and 2, the time delay is negative for the non-P case and positive for the P case. As k increases, however, the Equation (15) ceases to be valid and the evolution of the phase shift begins to depend numerically on the strength and relative difference of the potentials. A peak in time delay is noticed as a result of the inclusion of polarization in the low-energy region. For the partial wave $\ell = 3$, a completely different behavior of phase shift and time delay is obtained: The resonance condition is satisfied for both the ASW and DFT models. In addition, an abrupt phase leap through $\pi/2$ and an overall shift by π are noticed. Thus, a sharp peak in time delay is found. However, for ASW-P and DFT-P, the corresponding resonances have moved below the threshold as ascertained earlier, and hence no abrupt change in phase shift is observed. Consequently, the time delay profile has no sharp resonance peaks. A detailed analysis of the resonant cross-section is presented in Section 3.3. As the ℓ value increases, the angular momentum barrier increases, which prohibits the access of scattered waves in the region close to the origin. Consequently, the difference in the potential for the P and non-P cases will be less conspicuous.

3.2. Fano Parameterization of Resonances

Fano parametrization is employed for all model potentials to determine the resonant energy E_r and other parameters of the resonances [56]. The shape parameter q (from Equation (11)) characterizes the asymmetry of the resonance profile. It describes the interference between a pure resonant channel (with a Lorentzian shape profile) and a non-resonant background. Resonances are of different shapes based on the altering strength of this interference.

The shape parameters for the resonances in the ASW ($\ell = 3, 4, 5$) and ASW-P ($\ell = 4, 5, 6$) cross-section are shown in Table 2. The corresponding resonant partial wave cross-sections calculated are compared with the fitted cross-section in Figure 4. The q parameter value is large ($q = 28$) and positive for $\ell = 3$, which has a lower background cross-section (σ_o = 8.00 a_0^2) for the ASW potential. A high q value suggests that the interference between the resonant and direct (background) scattering is weak, leading to a Lorentzian shape of the cross-section. Furthermore, a weak coupling between the background and the resonant channel is found in the low σ_o. Relative to other resonances ($\ell = 4$ and 5), the $\ell = 3$ resonance shape is narrower ($\frac{\Gamma}{2} = 0.08 \times 10^{-3}$ a.u.) and more resembles the Lorentzian profile in ASW, as seen in Figure 4 (upper panel). Additionally, a small resonance width for $\ell = 3$ indicates a longer resonance lifetime. The q value remains

positive for $\ell = 4$ and 5 cases also; however, the values are found to approach zero. A lower value of q indicates a strong interference between resonant and direct scattering channels leading to asymmetric shape profiles, as is clear from Figure 4 (upper panel; $\ell = 4$ and 5). Furthermore, the $\ell = 4$ and $\ell = 5$ resonances are weak, indicating their shorter lifetimes.

For ASW-P (Figure 4 (lower panel)), no resonance is obtained for $\ell = 3$. From Table 2, it can be seen that when polarization is introduced to the ASW potential, the q value for $\ell = 4$ partial wave decreases from 2.69 to -19.30. Also, a considerable lowering of σ_o and resonance width values is noted. This indicates that the $\ell = 4$ resonance becomes sharper with the addition of polarization. For $\ell = 5$, the q value goes from 1.19 to 3.90 when the polarization is added and a decrease in the σ_o and Γ value is also observed. The resonance for $\ell = 6$ in ASW-P yields a q value of 1.69. Also, among the ASW-P resonances, the maximum σ_o and minimum Γ values are determined for $\ell = 6$, indicating an asymmetric and weaker resonance.

Table 2. Fano parameters of resonances using ASW and ASW-P model potential.

Model Potential	ℓ	Fano Parameters			
		E_r	q	$\frac{\Gamma}{2}$	σ_o
		a.u.		$\times 10^{-3}$ a.u.	a_0^2
ASW	3	0.0092	28.00	0.08	8.00
	4	0.0795	2.69	10.40	82.00
	5	0.1620	1.19	31.00	148.00
ASW-P	4	0.0524	−419.30	4.40	2.90
	5	0.1380	3.90	26.00	29.00
	6	0.2350	1.69	60.00	76.00

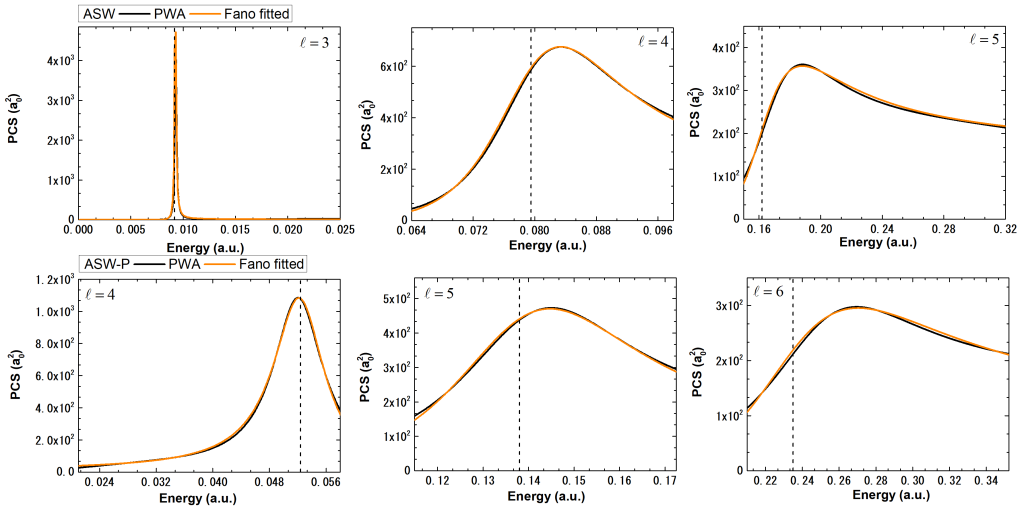

Figure 4. Comparison of $e-C_{60}$ elastic scattering resonant cross-sections calculated using PWA (black) for ASW (**upper panel**) and ASW-P (**lower panel**) with their Fano fitting profiles (orange). Vertical lines indicate the resonant energies E_r.

We also perform the Fano fitting analysis of the resonances obtained from the DFT and DFT-P model potential and the resulting values of the Fano parameters are listed in Table 3. In Figure 5, the fitted profiles for DFT (upper panel) and DFT-P (lower panel) are shown. The parametric values evolve very differently from DFT to DFT-P. In DFT, a resonance is noted for the partial wave $\ell = 3$, which yields $q = 6.23$ and a considerably large background cross-section $\sigma_o = 135a_0^2$. Consequently, the resonant shape is asymmetric. A resonance exists for $\ell = 1$ in DFT-P with energy $E_r = 0.0013$ a.u., $q = 2.48$, $\sigma_o = 920a_0^2$, and its asymmetry suggests a larger background cross-section. A common set of resonances for partial waves ($\ell = 4$, 7, 8, and 12) is shown in DFT and DFT-P. The q value increases from

1.65 to 2.79 for $\ell = 4$ when the polarization effect is added. Furthermore, decreases both in the resonant width and background cross-section imply that for $\ell = 4$ the polarization effect sharpens the resonance. When polarization effects are taken into account, the q value for $\ell = 7$ rises from -21.20 to -9.30, while for $\ell = 8$, the q value falls from 12.45 to -15.25. From Table 3, one notes that the resonance width is the narrowest for $\ell = 12$ in both DFT and DFT-P implying a prolonged lifetime. The corresponding q values for DFT and DFT-P are -5.60 and -4.53, respectively.

We remark that the lifetimes of these resonances, as derivable from their line widths, will affect the scattering time delay in general, since the electron will be transiently captured in these resonance states before arriving at the detector.

Table 3. Fano parameters of resonances using DFT and DFT-P model potential.

Model Potential	ℓ	Fano Parameters			
		E_r	q	$\frac{\Gamma}{2}$	σ_o
		a.u.		$\times 10^{-3}$ a.u.	a_0^2
DFT	3	0.0080	6.23	0.60	135.00
	4	0.0340	1.65	11.40	359.00
	7	0.1050	−21.20	2.50	2.00
	8	0.2120	12.45	28.20	3.20
	12	0.3414	−5.60	0.09	12.00
DFT-P	1	0.0013	2.48	1.35	920.00
	4	0.0258	2.79	5.50	228.00
	7	0.0818	−9.30	0.75	13.10
	8	0.1920	−15.25	20.60	2.40
	12	0.3109	−4.53	0.50	16.70

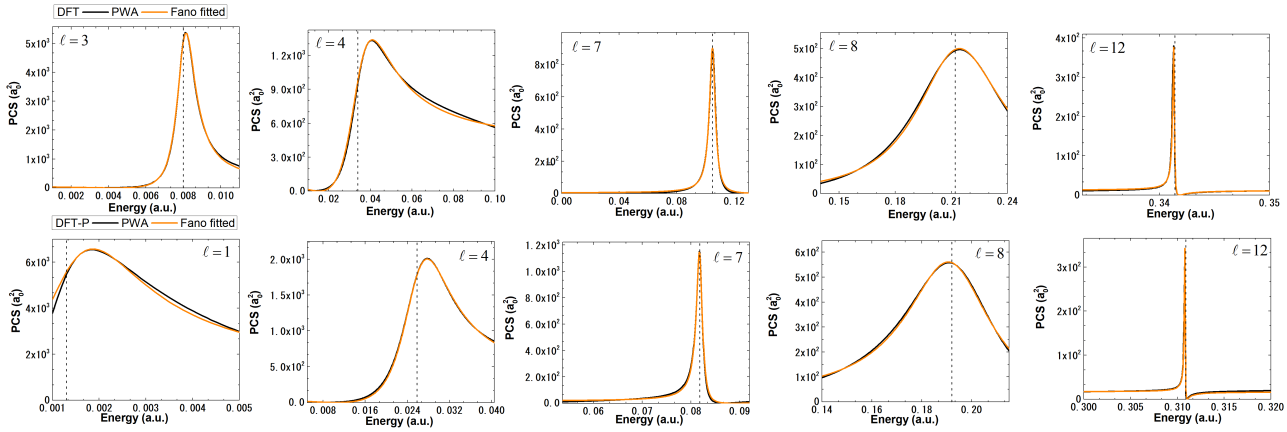

Figure 5. Comparison of $e-C_{60}$ elastic scattering resonant cross-sections calculated using PWA (black) in DFT (**upper panel**) and DFT-P (**lower panel**) with their Fano profiles (orange). Vertical lines indicate the resonant energies E_r.

3.3. Resonant Phase Shift and Time Delay

In Figure 6, the scattering phase shift and EWS time delay (using Equation (13)) are plotted for the resonant partial waves of ASW (upper panel) and ASW-P (lower panel) model potentials. The vertical lines indicate the corresponding resonant energies, which are obtained from the Fano analysis. First, we discuss the Non-P case (Figure 6, upper panel). The phase shift for $\ell = 3$ partial wave shows an abrupt $\pi/2$ jump and a sweep by π radian within a short energy range. As a result, the time delay sharply peaks as shown in Figure 6 (upper panel for $\ell = 3$). Subsequent partial waves ($\ell = 4$ and 5) also meet the resonant condition but comparatively weakly. For these weaker resonances, the magnitude of the phase shift is less than π across the resonance. The resonant time delay for the $\ell = 3$ partial wave is 410.45 femtoseconds (fs). This indicates that at this resonance, the electron stays in

the vicinity of the scatterer for quite a while. Resonant energy and the corresponding time delay values for the resonant partial waves are listed in Table 4. According to Table 4, the resonant time delay drops gradually for partial waves having higher angular momentum quantum numbers. A study by Amusia et al. [2], using the Dirac bubble potential model to describe fullerene, reported a similar trend in the time delay profile. In the ASW-P case (Figure 6, lower panel), $\ell = 3$ partial wave is non-resonant, but $\ell = 4$, 5, and 6 are resonant. The strongest resonance is observed for $\ell = 4$, having a delay value of 11.09 fs at the resonant energy $E_r = 0.0524$ a.u. This is followed by a smaller resonant time delay of 1.89 fs for $\ell = 5$ and 0.75 fs for $\ell = 6$. A progressive reduction in the resonant time delay is observed for larger angular momentum partial waves, similar to the trend in the ASW case.

As analyzed in Section 3.1, a small hump appears in the phase shift near zero energy due to the polarization effect. Consequent to this, a smaller peak in the time delay is seen in the ASW-P case, which is absent in the ASW case. For the $\ell = 4$ partial wave, the peak in time delay due to polarization is at 0.0524 a.u., and for $\ell = 5$ and $\ell = 6$, respectively, at 0.1380 a.u. and at 0.2350 a.u. Noticeably, although the phase shift is less sensitive to the polarization effect, an amplified feature is noted in time delay. This suggests that the time delay is more sensitive to changes in the potential compared to other scattering parameters.

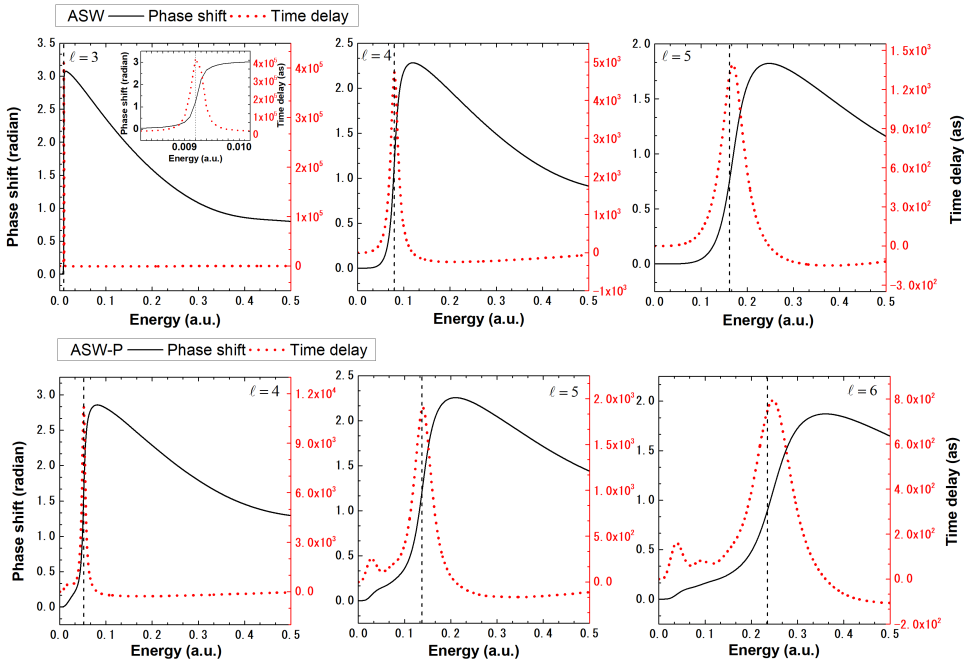

Figure 6. Resonant partial wave scattering phase shift (solid black) and EWS time delay (dashed red) plotted for ASW (**upper panel**) and ASW-P (**lower panel**) potentials. The phase shift is linked to the left axis and the time delay is linked to the right axis. Vertical line indicates the resonant energies E_r.

Table 4. Resonant energy and time delay for ASW and ASW-P case.

Resonant Partial Wave	ASW		ASW-P	
ℓ	Energy (a.u.)	Time Delay (fs)	Energy (a.u.)	Time Delay (fs)
3	0.0092	410.45	–	–
4	0.0795	4.73	0.0524	11.09
5	0.1620	1.32	0.1380	1.89
6	–	–	0.2350	0.75

For the $e-C_{60}$ interaction modeled by DFT, more resonances are seen. This is, as noted before, because of the intrinsic diffused shape and a deeper well in the DFT model. Phase shifts and the corresponding time delay profiles of resonant partial waves are shown in Figure 7. We first analyze the DFT case without polarization (Figure 7, upper panel). Here,

the resonance condition is satisfied for the partial waves $\ell = 3$, 4, 7, 8, and 12. As seen, $\ell = 12$ exhibits the sharpest resonance, followed by ℓ =3, 7, 4, and 8. The longest resonant delay is noted at $E_r = 0.3414$ a.u. for $\ell = 12$ with $\tau_{\ell=12} = 227.29$ fs. At $E_r = 0.2120$ a.u., the shortest resonant time delay of 1.63 fs is observed for $\ell = 8$ partial wave. Details of resonant energy and time delay values are given in Table 5. From Figure 7 (lower panel), the polarization-added DFT model (DFT-P) exhibits five notable resonances, just as in the DFT case. Here, a near-threshold resonance is obtained for $\ell = 1$, for which the resonant energy and time delay values are 0.0013 a.u. and 29.68 fs, respectively. Next, the resonance condition is attained for partial wave $\ell = 4$, followed by $\ell = 7$, 8, and 12. Similar to the DFT case, a steep jump in phase shift is obtained for $\ell = 12$, producing the maximum resonant delay value of 237.53 fs at the energy $E_r = 0.3109$ a.u. A steady jump in the phase is seen for the partial wave with $\ell = 7$ which induces a time delay value of 65.48 fs, while for $\ell = 4$ the resonant time delay is 8.49 fs. In comparison, the phase shift change is relatively small for $\ell = 8$ resulting in the lowest resonant time delay of 2.26 fs. For the case with polarization, however, there is a slight decrease in the resonant energy compared to the non-P case. This is because, as previously mentioned, the attractive polarization potential lowers the potential barrier. Similar to the ASW analysis, a very small bump in time delay in DFT-P for $\ell = 8$ is found which is likely induced by the polarization effect of C_{60}. For the remaining partial waves, since the resonances dominate changes due to the polarization effect, the humps in the phase shift and corresponding smaller peaks in the delay are masked.

Table 5. Resonant energy and time delay for DFT and DFT-P case.

Resonant Partial Wave ℓ	DFT		DFT-P	
	Energy (a.u.)	**Time Delay (fs)**	**Energy (a.u.)**	**Time Delay (fs)**
1	–	–	0.0013	29.68
3	0.0080	81.60	–	–
4	0.0340	4.12	0.0258	8.49
7	0.1050	18.79	0.0818	65.48
8	0.2120	1.63	0.1920	2.26
12	0.3414	227.29	0.3109	237.53

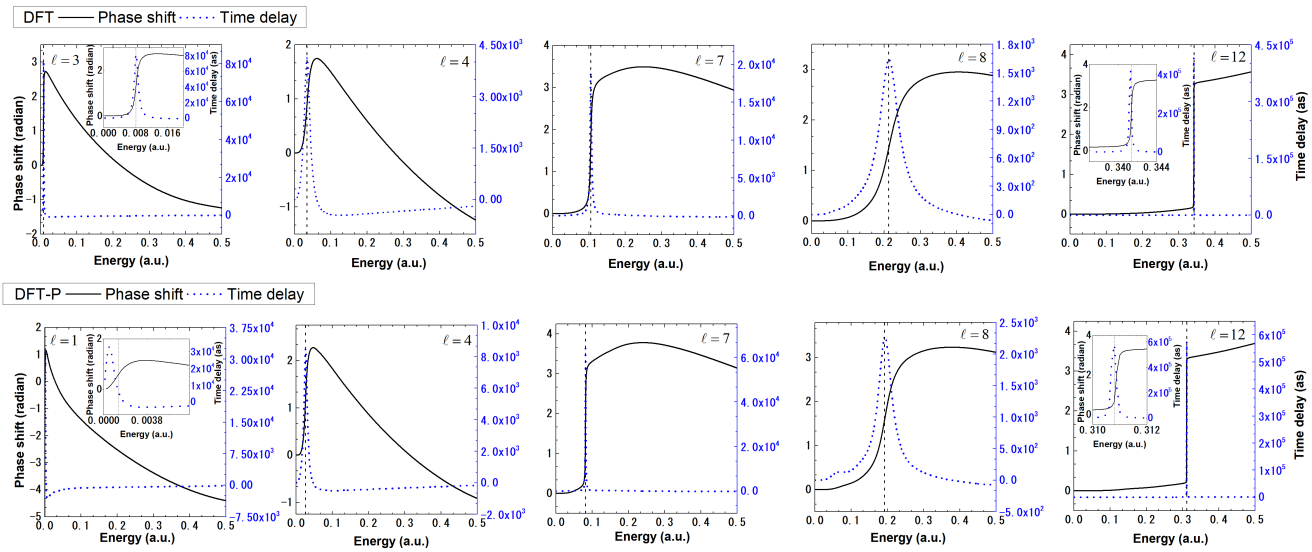

Figure 7. Resonant partial wave scattering phase shift (solid black) and EWS time delay (dashed blue) are plotted for DFT (**upper panel**) and DFT-P (**lower panel**) potentials. The phase shift is linked to the left axis and the time delay is linked to the right axis. Vertical lines indicate the resonant energies E_r.

3.4. Average Time Delay

The time delay results presented above are for individual partial waves, which can not be experimentally observed. However, the average time delay is the quantity that can be measured in principle. Figure 8 shows the average delay, computed using Equation (14), of the $e-C_{60}$ elastic process in (a) ASW, ASW-P and (b) DFT, DFT-P. The average time delay profiles exhibit all of the resonant peaks that are seen in TCS, as expected. For ASW and ASW-P cases (Figure 8a), while energy $E \to 0$, the average time delay tends to negative infinity. The $s-$wave time delay profile dominates the average delay behavior in the low energy limit since the low energy collision is dominated by the s-wave scattering. For both the ASW and ASW-P cases, a progressive decline in the delay peak value is noted. The contribution of partial wave $\ell = 1$ is responsible for a very small hump in the ASW-P profile that is observed in the energy limit to zero. The average time delay in DFT also contains all of the resonant partial wave peaks (Figure 8b), much like in the ASW case. Because of the dominant influence of the $\ell = 0$ partial wave, the average time delay here also approaches negative infinity in the low energy limit, in accordance with the Wigner threshold law. We recall the partial wave $\ell = 12$ yielded the largest EWS delay value in both the DFT and DFT-P cases. Accordingly, the average delay also shows very steep peaks for the same partial wave. Structures from a common set of partial waves are observed in both the DFT and DFT-P frames where the polarization effect causes an enhancement of the time delay and an energy-dependent red-shift of the peak position is noted.

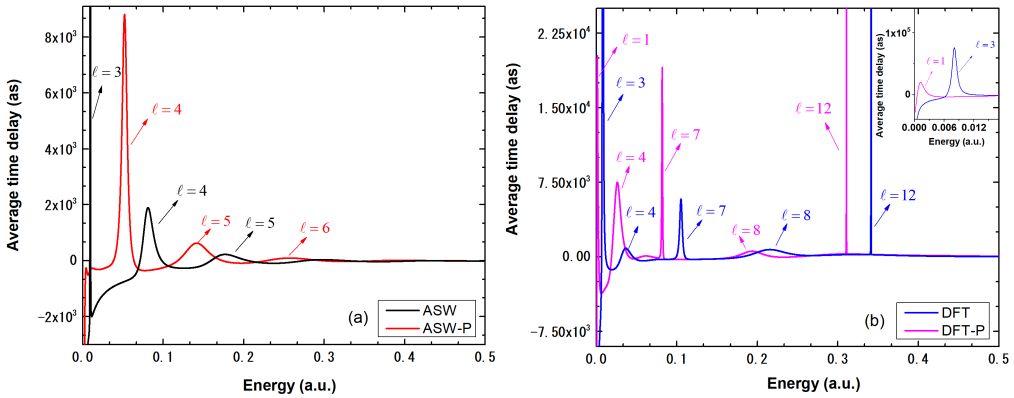

Figure 8. Average time delay of $e-C_{60}$ elastic scattering using model potentials (**a**) ASW (black) and ASW-P (red) (**b**) DFT (blue) and DFT-P (magenta). The average time delay behavior magnified in the low energy limit is shown in the inset for the DFT case. The resonant time delays are labeled with the corresponding partial wave's angular momentum quantum number.

4. Conclusions

The present study focuses on investigating electron elastic scattering from a C_{60} molecule using the DFT and ASW model potentials. This study reports, for the first time, positive humps in the EWS time delay for resonant partial wave channels, which are attributed to the polarization effect. Furthermore, the sensitivity of the time delay versus other scattering parameters, and changes in the interaction potential are revealed in the study. A similar observation was made earlier for photoionization, where the angular distribution asymmetry parameter (β) was found to be less sensitive to the interaction model used compared to the ionization time delay [60,61]. The present work reaffirms such peculiar delicateness of the time delay as observable but in the context of electron scattering.

Using ultrafast two-photon pump-probe laser pulses, measurements of time delay in photoionization is now possible [1]. If experimental technology allows, it may also be possible to employ similar approaches to measure the time delay in electron scattering. An electron pulse can be sent to the target to scatter in a spherical pulse (scattering pulse), which can be followed by a probe laser pulse time-delayed from the original pulse in a controllable manner. This general technique can be realized either on an interferometric

or a streaking track, as routinely conducted nowadays in photoelectron chronoscopy. The current study may generate a preliminary impetus to this goal.

Author Contributions: Conceptualization, A.R., J.J., H.R.V. and H.S.C.; methodology, A.R.; software, A.R. and R.S.; validation, J.J., H.R.V. and H.S.C.; formal analysis, A.R., J.J., H.R.V. and H.S.C.; investigation, A.R., J.J., H.R.V. and H.S.C.; resources, A.R., R.S., J.J., H.R.V. and H.S.C.; data curation, A.R., R.S., J.J., H.R.V. and H.S.C.; writing—original draft preparation, A.R.; writing—review and editing, A.R., J.J., H.R.V. and H.S.C.; visualization, A.R., R.S., J.J., H.R.V. and H.S.C.; supervision, J.J., H.R.V. and H.S.C.; project administration, J.J., H.R.V. and H.S.C.; funding acquisition, J.J., H.R.V. and H.S.C. All authors have read and agreed to the published version of the manuscript.

Funding: This research was funded by SERB-CRG Project grant number CRG/2022/000191, India (J.J.), SERB-CRG Project grant number CRG/2022/002309, India (H.R.V.), and by the US National Science Foundation Grant No. PHY-2110318 (H.S.C.).

Data Availability Statement: The original contributions presented in the study are included in the article.

Conflicts of Interest: The authors declare no conflicts of interest.

References

1. Schultze, M.; Fieß, M.; Karpowicz, N.; Gagnon, J.; Korbman, M.; Hofstetter, M.; Neppl, S.; Cavalieri, A.L.; Komninos, Y.; Mercouris, T.; et al. Delay in photoemission. *Science* **2010**, *328*, 1658–1662. [CrossRef]
2. Amusia, M.Y.; Baltenkov, A. Time delay in electron-C_{60} elastic scattering in a dirac bubble potential model. *J. Phys. B At. Mol. Opt. Phys.* **2018**, *52*, 015101. [CrossRef]
3. Amusia, M.Y.; Baltenkov, A.S.; Woiciechowski, I. Partial time delays in elastic electron scattering by rectangular potential well with arising discrete levels. *Eur. Phys. J. D* **2019**, *73*, 265. [CrossRef]
4. Amusia, M.Y.; Baltenkov, A. Time delay of slow electrons-endohedral elastic scattering. *Fullerenes Nanotub. Carbon Nanostruct.* **2020**, *28*, 10–13. [CrossRef]
5. Eisenbud, L. *The Formal Properties of Nuclear Collisions*; Princeton University: Princeton, NJ, USA, 1948.
6. Wigner, E.P. Lower limit for the energy derivative of the scattering phase shift. *Phys. Rev.* **1955**, *98*, 145. [CrossRef]
7. Smith, F.T. Lifetime matrix in collision theory. *Phys. Rev.* **1960**, *118*, 349. [CrossRef]
8. Amusia, M.Y.; Baltenkov, A.; Woiciechowski, I. Wigner time delay of particles elastically scattered by a cluster of zero-range potentials. *Phys. Rev. A* **2022**, *105*, 012807. [CrossRef]
9. Aiswarya, R.; Jose, J. An Investigation of the Resonant and Non-Resonant Angular Time Delay of e-C_{60} Elastic Scattering. *Atoms* **2022**, *10*, 77.
10. Deshmukh, P.; Banerjee, S. Time delay in atomic and molecular collisions and photoionisation/photodetachment. *Int. Rev. Phys. Chem.* **2021**, *40*, 127–153. [CrossRef]
11. Guenot, D.; Klünder, K.; Arnold, C.; Kroon, D.; Dahlström, J.M.; Miranda, M.; Fordell, T.; Gisselbrecht, M.; Johnsson, P.; Mauritsson, J.; et al. Photoemission-time-delay measurements and calculations close to the 3 s-ionization-cross-section minimum in ar. *Phys. Rev. A* **2012**, *85*, 053424. [CrossRef]
12. Wang, H.; Chini, M.; Chen, S.; Zhang, C.H.; He, F.; Cheng, Y.; Wu, Y.; Thumm, U.; Chang, Z. Attosecond time-resolved autoionization of argon. *Phys. Rev. Lett.* **2010**, *105*, 143002. [CrossRef]
13. Bain, R.; Bardsley, J. Shape resonances in atom-atom collisions. I. Radiative association. *J. Phys. B At. Mol. Phys.* **1972**, *5*, 277. [CrossRef]
14. Yao, X.C.; Qi, R.; Liu, X.P.; Wang, X.Q.; Wang, Y.X.; Wu, Y.P.; Chen, H.Z.; Zhang, P.; Zhai, H.; Chen, Y.A.; et al. Degenerate Bose gases near ad-wave shape resonance. *Nat. Phys.* **2019**, *15*, 570–576. [CrossRef]
15. Bianconi, A.; Congiu-Castellano, A.; Durham, P.; Hasnain, S.; Phillips, S. The CO bond angle of carboxymyoglobin determined by angular-resolved XANES spectroscopy. *Nature* **1985**, *318*, 685–687. [CrossRef] [PubMed]
16. Bianconi, A.; Petersen, H.; Brown, F.C.; Bachrach, R. K-shell photoabsorption spectra of N_2 and N_2O using synchrotron radiation. *Phys. Rev. A* **1978**, *17*, 1907. [CrossRef]
17. Bianconi, A. On the possibility of new high T_c superconductors by producing metal heterostructures as in the cuprate perovskites. *Solid State Commun.* **1994**, *89*, 933–936. [CrossRef]
18. Miroshnichenko, A.E.; Flach, S.; Kivshar, Y.S. Fano resonances in nanoscale structures. *Rev. Mod. Phys.* **2010**, *82*, 2257. [CrossRef]
19. Chai, Y.; Guo, T.; Jin, C.; Haufler, R.E.; Chibante, L.F.; Fure, J.; Wang, L.; Alford, J.M.; Smalley, R.E. Fullerenes with metals inside. *J. Phys. Chem.* **1991**, *95*, 7564–7568. [CrossRef]
20. Deshmukh, P.; Jose, J.; Varma, H.; Manson, S. Electronic structure and dynamics of confined atoms. *Eur. Phys. J. D* **2021**, *75*, 166. [CrossRef]
21. Hartman, K.B.; Wilson, L.J.; Rosenblum, M.G. Detecting and treating cancer with nanotechnology. *Mol. Diagn. Ther.* **2008**, *12*, 1–14. [CrossRef]

22. Shu, C.Y.; Ma, X.Y.; Zhang, J.F.; Corwin, F.D.; Sim, J.H.; Zhang, E.Y.; Dorn, H.C.; Gibson, H.W.; Fatouros, P.P.; Wang, C.R.; et al. Conjugation of a water-soluble gadolinium endohedral fulleride with an antibody as a magnetic resonance imaging contrast agent. *Bioconj. Chem.* **2008**, *19*, 651–655. [CrossRef] [PubMed]
23. Ross, R.B.; Cardona, C.M.; Guldi, D.M.; Sankaranarayanan, S.G.; Reese, M.O.; Kopidakis, N.; Peet, J.; Walker, B.; Bazan, G.C.; Van Keuren, E.; et al. Endohedral fullerenes for organic photovoltaic devices. *Nat. Mater.* **2009**, *8*, 208–212. [CrossRef]
24. Hedley, G.J.; Ward, A.J.; Alekseev, A.; Howells, C.T.; Martins, E.R.; Serrano, L.A.; Cooke, G.; Ruseckas, A.; Samuel, I.D. Determining the optimum morphology in high-performance polymer-fullerene organic photovoltaic cells. *Nat. Commun.* **2013**, *4*, 2867. [CrossRef] [PubMed]
25. Harneit, W.; Boehme, C.; Schaefer, S.; Huebener, K.; Fostiropoulos, K.; Lips, K. Room temperature electrical detection of spin coherence in C_{60}. *Phys. Rev. Lett.* **2007**, *98*, 216601. [CrossRef] [PubMed]
26. Zhao, Y.; Kim, Y.H.; Dillon, A.; Heben, M.; Zhang, S. Hydrogen storage in novel organometallic buckyballs. *Phys. Rev. Lett.* **2005**, *94*, 155504. [CrossRef] [PubMed]
27. Zadik, R.H.; Takabayashi, Y.; Klupp, G.; Colman, R.H.; Ganin, A.Y.; Potočnik, A.; Jeglič, P.; Arčon, D.; Matus, P.; Kamarás, K.; et al. Optimized unconventional superconductivity in a molecular Jahn-Teller metal. *Sci. Adv.* **2015**, *1*, e1500059. [CrossRef] [PubMed]
28. Campbell, E.K.; Holz, M.; Gerlich, D.; Maier, J.P. Laboratory confirmation of C_{60}^+ as the carrier of two diffuse interstellar bands. *Nature* **2015**, *523*, 322–323. [CrossRef] [PubMed]
29. Cami, J.; Bernard-Salas, J.; Peeters, E.; Malek, S.E. Detection of C_{60} and C_{70} in a young planetary nebula. *Science* **2010**, *329*, 1180–1182. [CrossRef]
30. Cordiner, M.; Linnartz, H.; Cox, N.; Cami, J.; Najarro, F.; Proffitt, C.; Lallement, R.; Ehrenfreund, P.; Foing, B.; Gull, T.; et al. Confirming interstellar C_{60}^+ using the hubble space telescope. *Astrophys. J. Lett.* **2019**, *875*, L28. [CrossRef]
31. Pazourek, R.; Nagele, S.; Burgdörfer, J. Attosecond chronoscopy of photoemission. *Rev. Mod. Phys.* **2015**, *87*, 765. [CrossRef]
32. Magrakvelidze, M.; Anstine, D.M.; Dixit, G.; Madjet, M.E.A.; Chakraborty, H.S. Attosecond structures from the molecular cavity in fullerene photoemission time delay. *Phys. Rev. A* **2015**, *91*, 053407. [CrossRef]
33. Biswas, S.; Trabattoni, A.; Rupp, P.; Magrakvelidze, M.; Madjet, M.E.A.; De Giovannini, U.; Castrovilli, M.C.; Galli, M.; Liu, Q.; Månsson, E.P.; et al. Attosecond correlated electron dynamics at C_{60} giant plasmon resonance. *arXiv* **2021**, arXiv:2111.14464.
34. Amusia, M.Y.; Chernysheva, L.V. Time delay of photoionization by Endohedrals. *JETP Lett.* **2020**, *112*, 219–224. [CrossRef]
35. Dixit, G.; Chakraborty, H.S.; Madjet, M.E.A. Time delay in the recoiling valence photoemission of ar endohedrally confined in C_{60}. *Phys. Rev. Lett.* **2013**, *111*, 203003. [CrossRef] [PubMed]
36. Thuppilakkadan, A.; Banerjee, S.; Varma, H.R. Modifications in the angular photoemission time delay in Ar@ $C_{60}^{q=-1}$: Coulomb confinement resonance as an amplifier of the spin-orbit-interaction-activated interchannel coupling effect. *Phys. Rev. A* **2023**, *107*, 052804. [CrossRef]
37. Winstead, C.; McKoy, V. Elastic electron scattering by fullerene C_{60}. *Phys. Rev. A* **2006**, *73*, 012711. [CrossRef]
38. Hargreaves, L.; Lohmann, B.; Winstead, C.; McKoy, V. Elastic scattering of intermediate-energy electrons from C_{60} molecules. *Phys. Rev. A* **2010**, *82*, 062716. [CrossRef]
39. Gianturco, F.; Lucchese, R.; Sanna, N. Computed elastic cross sections and angular distributions of low-energy electron scattering from gas phase C_{60} fullerene. *J. Phys. At. Mol. Opt. Phys.* **1999**, *32*, 2181. [CrossRef]
40. Tanaka, H.; Boesten, L.; Onda, K.; Ohashi, O. Crossed-beam experiment for the scattering of low energy electrons from gas phase C_{60}. *J. Phys. Soc. Jpn.* **1994**, *63*, 485–492. [CrossRef]
41. Tanaka, H.; Hoshino, M.; Brunger, M. Elastic and inelastic scattering of low-energy electrons from gas-phase C_{60}: Elastic scattering angular distributions and coexisting solid-state features revisited. *Eur. Phys. J. D* **2021**, *75*, 293. [CrossRef]
42. Madjet, M.E.; Chakraborty, H.S.; Rost, J.M.; Manson, S.T. Photoionization of C_{60}: A model study. *J. Phys. B At. Mol. Opt. Phys.* **2008**, *41*, 105101. [CrossRef]
43. Choi, J.; Chang, E.; Anstine, D.M.; Madjet, M.E.A.; Chakraborty, H.S. Effects of exchange-correlation potentials on the density-functional description of C_{60} versus C_{240} photoionization. *Phys. Rev. A* **2017**, *95*, 023404. [CrossRef]
44. Dolmatov, V.; Cooper, M.; Hunter, M. Electron elastic scattering off endohedral fullerenes A@ C_{60}: The initial insight. *J. Phys. B At. Mol. Opt. Phys.* **2014**, *47*, 115002. [CrossRef]
45. Amusia, M.Y.; Chernysheva, L.; Dolmatov, V. Angle-differential elastic-electron scattering off C_{60}: A simple semi-empirical theory versus experiment. *J. Phys. B At. Mol. Opt. Phys.* **2019**, *52*, 085201. [CrossRef]
46. Baltenkov, A.; Manson, S.; Msezane, A. Jellium model potentials for the C_{60} molecule and the photoionization of endohedral atoms, A@C_{60}. *J. Phys. B At. Mol. Opt. Phys.* **2015**, *48*, 185103. [CrossRef]
47. Puska, M.J.; Nieminen, R.M. Photoabsorption of atoms inside C_{60}. *Phys. Rev. A* **1993**, *47*, 1181. [CrossRef] [PubMed]
48. Kohn, W.; Sham, L.J. Self-consistent equations including exchange and correlation effects. *Phys. Rev.* **1965**, *140*, A1133. [CrossRef]
49. Dolmatov, V.; Amusia, M.Y.; Chernysheva, L. Effects of target polarization in electron elastic scattering off endohedral A@C_{60}. *Phys. Rev. A* **2017**, *95*, 012709. [CrossRef]
50. Aiswarya, R.; Shaik, R.; Jose, J.; Varma, H.R.; Chakraborty, H.S. Simultaneous real and momentum space electron diffraction from a fullerene molecule. *arXiv* **2024**, arXiv:2402.08103.
51. Rüdel, A.; Hentges, R.; Becker, U.; Chakraborty, H.S.; Madjet, M.E.; Rost, J.M. Imaging delocalized electron clouds: Photoionization of C_{60} in fourier reciprocal space. *Phys. Rev. Lett.* **2002**, *89*, 125503. [CrossRef]
52. Thijssen, J.M. *Computational Physics*; Cambridge University Press: Cambridge, UK, 2007.

53. Joachain, C.J. *Quantum Collision Theory*; North Holland Publishing Company: Amsterdam, The Netherlands, 1975.
54. Zhang, S.; Jin, J. *Computation of Special Functions*; Wiley: New York, NY, USA, 1996.
55. Scully, S.; Emmons, E.; Gharaibeh, M.; Phaneuf, R.; Kilcoyne, A.; Schlachter, A.; Schippers, S.; Müller, A.; Chakraborty, H.; Madjet, M.; et al. Photoexcitation of a volume plasmon in C_{60} ions. *Phys. Rev. Lett.* **2005**, *94*, 065503. [CrossRef] [PubMed]
56. Fano, U. Effects of configuration interaction on intensities and phase shifts. *Phys. Rev.* **1961**, *124*, 1866. [CrossRef]
57. Sarswat, S.; Aiswarya, R.; Jose, J. Shannon entropy of resonant scattered state in the e-C_{60} elastic collision. *J. Phys. B At. Mol. Opt. Phys.* **2022**, *55*, 055003. [CrossRef]
58. Amusia, M.Y.; Baltenkov, A.; Krakov, B. Photodetachment of negative C_{60}^- ions. *Phys. Lett. A* **1998**, *243*, 99–105. [CrossRef]
59. Wigner, E.P. On the behavior of cross sections near thresholds. *Phys. Rev.* **1948**, *73*, 1002. [CrossRef]
60. Baral, S.; Jose, J.; Deshmukh, P.; Manson, S. 6p Cooper minima in the photoionization in high-Z atoms. In Proceedings of the APS Division of Atomic, Molecular and Optical Physics Meeting Abstracts, Orlando, FL, USA, 30 May–3 June 2022.
61. Deshmukh, P.; Mandal, A.; Saha, S.; Kheifets, A.; Dolmatov, V.; Manson, S. Attosecond time delay in the photoionization of endohedral atoms A@C_{60}: A probe of confinement resonances. *Phys. Rev. A* **2014**, *89*, 053424. [CrossRef]